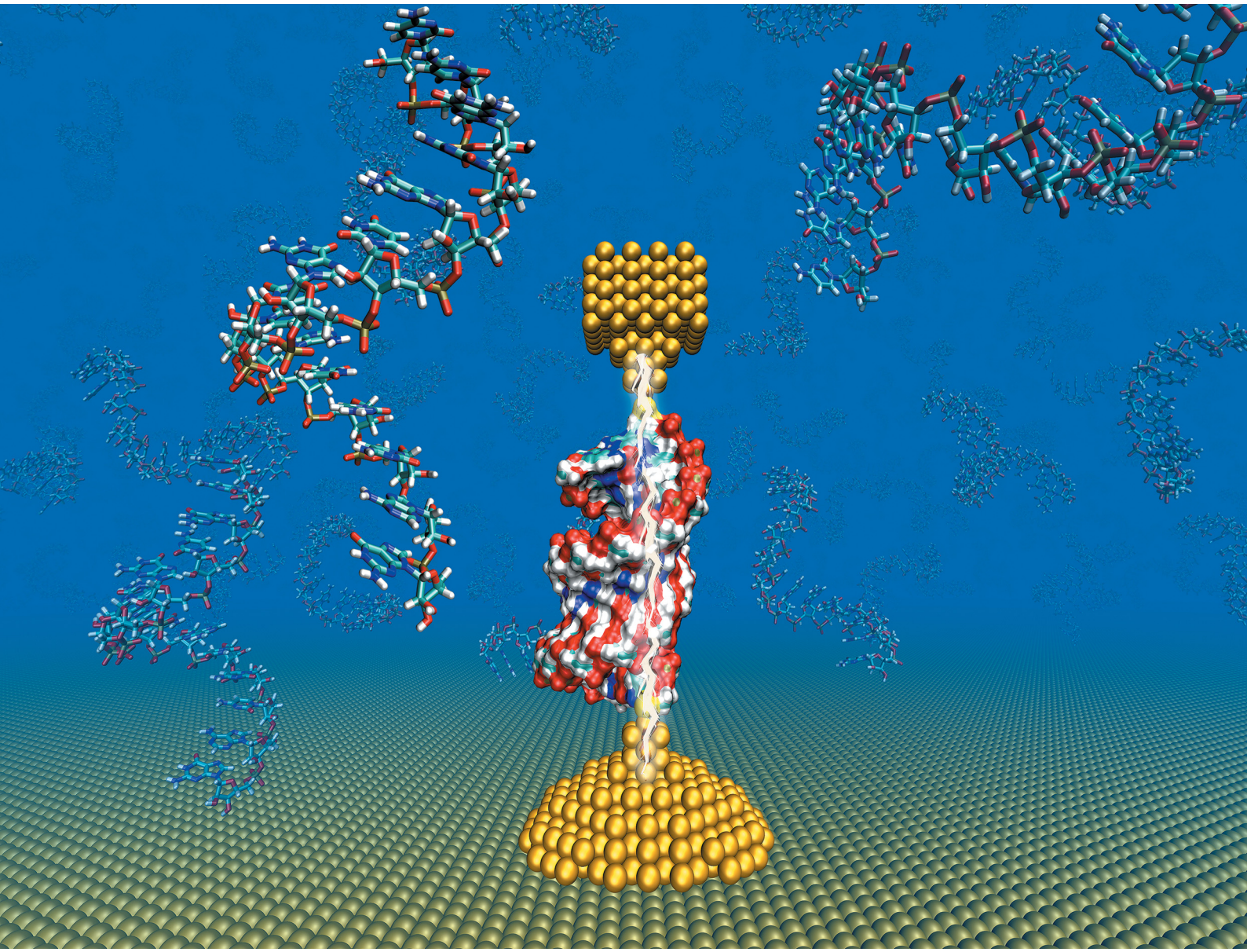
Volume 6
Number 8
August 2021
Pages 577–670

Nanoscale Horizons

The home for rapid reports of exceptional significance in nanoscience and nanotechnology

rsc.li/nanoscale-horizons



ISSN 2055-6756

ROYAL SOCIETY OF CHEMISTRY

COMMUNICATION

Ersin Emre Oren, M. P. Anantram *et al.*

Role of intercalation in the electrical properties of nucleic acids for use in molecular electronics

NCNST

Nanoscale Horizons

ROYAL SOCIETY OF CHEMISTRY

COMMUNICATION

View Article Online
View Journal | View Issue

Published on 08 June 2021. Downloaded by University of Washington on 9/13/2024 10:54:56 PM.

Check for updates

Cite this: *Nanoscale Horiz.*, 2021, 6, 651

Received 12th April 2021,
Accepted 7th June 2021

DOI: 10.1039/d1nh00211b

rsc.li/nanoscale-horizons

Role of intercalation in the electrical properties of nucleic acids for use in molecular electronics†

Hashem Mohammad, ‡[a] Busra Demir, ‡[bc] Caglanaz Akin, [bc] Binquan Luan, [d] Joshua Hihath, [e] Ersin Emre Oren *[bc] and M. P. Anantram*[a]

Intercalating ds-DNA/RNA with small molecules can play an essential role in controlling the electron transmission probability for molecular electronics applications such as biosensors, single-molecule transistors, and data storage. However, its applications are limited due to a lack of understanding of the nature of intercalation and electron transport mechanisms. We addressed this long-standing problem by studying the effect of intercalation on both the molecular structure and charge transport along the nucleic acids using molecular dynamics simulations and first-principles calculations coupled with the Green's function method, respectively. The study on anthraquinone and anthraquinone–neomycin conjugate intercalation into short nucleic acids reveals some universal features: (1) the intercalation affects the transmission by two mechanisms: (a) inducing energy levels within the bandgap and (b) shifting the location of the Fermi energy with respect to the molecular orbitals of the nucleic acid, (2) the effect of intercalation was found to be dependent on the redox state of the intercalator: while oxidized anthraquinone decreases, reduced anthraquinone increases the conductance, and (3) the sequence of the intercalated nucleic acid further affects the transmission: lowering the AT-region length was found to enhance the electronic coupling of the intercalator with GC bases, hence yielding an increase of more than four times in conductance. We anticipate our study to inspire designing intercalator–nucleic acid complexes for potential use in molecular electronics *via* creating a multi-level gating effect.

New concepts

Facilitated by the advance of synthetic biology, designer DNA with predetermined sequences can be readily synthesized for various applications (*e.g.*, biosensors, single molecule transistors and DNA storage) in the nascent field of molecular electronics. However, the lack of control of charge transport significantly limits its application in nanoelectronics. While experiments have shown that the conductivity of DNA can be adjusted *via* intercalation with organic molecules, the mechanism is still not established. In this work, using rigorous calculations, we addressed this problem by studying the effect of intercalation on both the molecular structure of and charge transport along the nucleic acids. We estimated the location of the Fermi energy using partial charge transfer analysis. This helped us show that the conductance of DNA can be altered depending on the redox state of the intercalator, induced energy levels, and the location of the Fermi energy. These results establish the theoretical basis for intercalation-regulated conductance and thus can guide the design of novel intercalator–nucleic acid systems for use in future molecular electronic devices.

Introduction

The electronic properties of DNA have attracted particular interest over the past 20 years[1] due to its long-range charge transport and self-assembly properties, making it a desirable nanoelectronics component. DNA consists of four main bases: guanine (G), cytosine (C), adenine (A), and thymine (T), and the stacking and pairing of these bases form a helical structure. The π–π interactions of the stacked bases lead to long-range charge transport. Simultaneously, due to its molecular recognition (exclusive base-pairing), sophisticated geometries can be precisely fabricated, overcoming the scaling challenges with solid-state/silicon-based electronics. Thus, the understanding of the electrical properties of DNA, either theoretically or experimentally, becomes a key factor for future device developments.

The last decade has witnessed clear demonstrations of the sensitivity of short oligonucleotides' electrical conductance

[a] *Department of Electrical Engineering, University of Washington, Seattle, WA, USA. E-mail: anantmp@uw.edu*
[b] *Bionanodesign Laboratory, Department of Biomedical Engineering, TOBB University of Economics and Technology, Ankara, Turkey. E-mail: eeoren@etu.edu.tr*
[c] *Department of Materials Science & Nanotechnology Engineering, TOBB University of Economics and Technology, Ankara, Turkey*
[d] *Computational Biological Center, IBM Thomas J. Watson Research, Yorktown Heights, NY 10598, USA*
[e] *Electrical and Computer Engineering Department, University of California Davis, Davis, CA, USA*

† Electronic supplementary information (ESI) available: Methods, computational details, binding energy calculations, AT-region length effect on energy and transmission. See DOI: 10.1039/d1nh00211b

‡ These authors contributed equally.

Published on 08 June 2021. Downloaded by University of Washington on 9/13/2024 10:54:56 PM.

(5 nm range) to chemical modification of the nucleotide,[2–4] conformational change,[5–8] and single base mismatch.[9] The ability to tune and control these factors has wide implications in electronics, sensors,[10–19] and sequencing.[20–22]

Intercalation is an insertion of small molecules between bases of a nucleic acid structure, triggering structural changes such as local unwinding and elongation.[23] Small molecules called intercalators are often used as anticancer drugs to inhibit nucleic acid replication[24] or as fluorescent markers to visualize the structure.[25] The interaction between intercalators and nucleic acids has been studied both experimentally and computationally.[26–31] Consequently, there has been growing interest in controlling nucleic acid conductance by adding intercalators.

Recently, a graphene quantum dot intercalator in a 59-base pair long abasic-DNA was found to enhance the charge transfer rate.[32] An 11-base pair DNA intercalated with coralyne showed three times larger conductance than the native DNA at negative biases.[33] However, other studies have shown a contrasting impact of intercalation on DNA conductance. Harashima *et al.*[34] demonstrated that intercalation using ethidium bromide increased the conductance by four times; they also showed that using Hoechst-33258 as a minor groove binder did not induce an increase in conductance on the same ds-DNA having 8 base pairs. On the other hand, an earlier experiment conducted by Wang *et al.*[35] demonstrated that the same intercalator (ethidium bromide) decreased the conductance of 20 base-pair long ds-DNA. Recently, Xiang *et al.*[36] reported that an anthraquinone (Aq) molecule directly attached to the end of the backbone of ds-DNA *via* an uracil (U) base could modify the conductance of a ds-DNA based on its redox state. In their experiment, they showed that the Aq moiety intercalated the complementary strand between the guanine bases, and the reduced state Aq yielded higher conductance, while the oxidized state Aq yielded lower conductance than the unmodified DNA. The experimental papers do not resolve the underlying mechanisms in a unified manner as exemplified from the literature. A recent modelling paper by Aggarwal *et al.*[37] reported the effect of ethidium and daunomycin intercalators on the conductance of 8 and 12 base-pair long DNA strands. They used *ab initio* calculations and showed that, upon intercalation, the conductance increases by one order of magnitude mainly due to reducing the twist angle between the intercalated base pairs, enhancing their structural alignment.

In this paper, we explore the fundamental pathways to alter the conductance of DNA upon intercalation, which is relevant to molecular electronics. We employ a combination of molecular dynamics (MD) simulations, density functional theory (DFT), and Green's function-based charge transport calculations. We focus on two different nucleic acids, ds-DNA and a DNA:RNA hybrid, both intercalated with Aq. We study the impact of the redox state, location, and quantity of intercalators in altering ds-DNA's electronic properties considering different measurement scenarios. We report a new approach to analyze the effect of intercalations on the Fermi energy using a partial charge transfer concept. Subsequently, we demonstrate that Aq intercalation in ds-DNA can increase or decrease the conductance, depending on the oxidation state, due to the following two reasons: (1) intercalation decreases the bandgap energy by inducing new energy levels within the bandgap region of the bare ds-DNA, either close to the HOMO region (reduced Aq case) or in the middle of the bandgap (oxidized Aq case), and (2) intercalation shifts the Fermi energy with respect to the HOMO of the intercalated ds-DNA. We also report that the effects of Aq intercalation on both ds-DNA and DNA:RNA hybrids are alike.

We additionally model intercalation by an anthraquinone–neomycin conjugate (AqNEO) in DNA:RNA hybrids as the binding stability was experimentally studied by Degtyareva *et al.*[38] Neomycin has been shown to increase the thermal stability of RNA duplexes[39] and also the binding affinity of the conjugated intercalator to DNA:RNA duplexes.[40] We show that the neomycin part of the conjugate, acting as a groove binder, has a small effect on the conductance, which agrees with the literature results.[34,35] We report that this is due to the indistinctive changes in the molecular orbitals around the HOMO region of the DNA:RNA hybrid.

The paper is organized as follows: first, we introduce the cases under study and discuss the structural impact of intercalation (MD results). We follow it with energy level analysis (quantum mechanics calculations). Then, we focus on the energy levels induced by the intercalators and their impact on transmission. Afterward, we study the effect of having two intercalators on altering electron transmission through DNA. After this focused analysis on the intercalator induced levels, we shift our attention to the overall conductance. Thus, we analyze the partial charge transfer rates to predict the Fermi energy for conductance comparisons. Finally, we study an additional case of a structure with a shorter AT region and illustrate key differences.

Results and discussion

We study a family of three structures: (1) Aq (both oxidized and reduced states) intercalation into a 15 base-pair ds-DNA with the sequence 3-G3A9G3-5. (2) Aq and AqNEO intercalation into a DNA:RNA hybrid having the same sequence, with the RNA strand formed by purines and the DNA formed by pyrimidines. (3) Aq (both oxidized and reduced states) intercalation into a ds-DNA with a shorter AT region, having the sequence 3-G3A3G3-5. We first focus on 1 and 2 (Fig. 1a) to understand the intrinsic effects of the intercalation on the strands. The 15 base-pair structures are expected to be comparatively resistive due to the high number of AT base pairs, creating a barrier for the charge to traverse the structure to the terminal guanines. Thus, as for the 3rd structure, we lowered the AT-region length from 9 to 3 base pairs. As will be shown, the effect of intercalation on both ds-DNA and the DNA:RNA hybrid is similar; hence, moving forward in the transport calculations, the discussion will focus on the ds-DNA system.

The exact location of intercalation is difficult to identify experimentally as Aq and its derivatives can reside between any consecutive base pairs depending on the molecular interactions between the intercalator molecule and the nucleic acids.[41,42]

 This journal is © The Royal Society of Chemistry 2021

Published on 08 June 2021. Downloaded by University of Washington on 9/13/2024 10:54:56 PM.

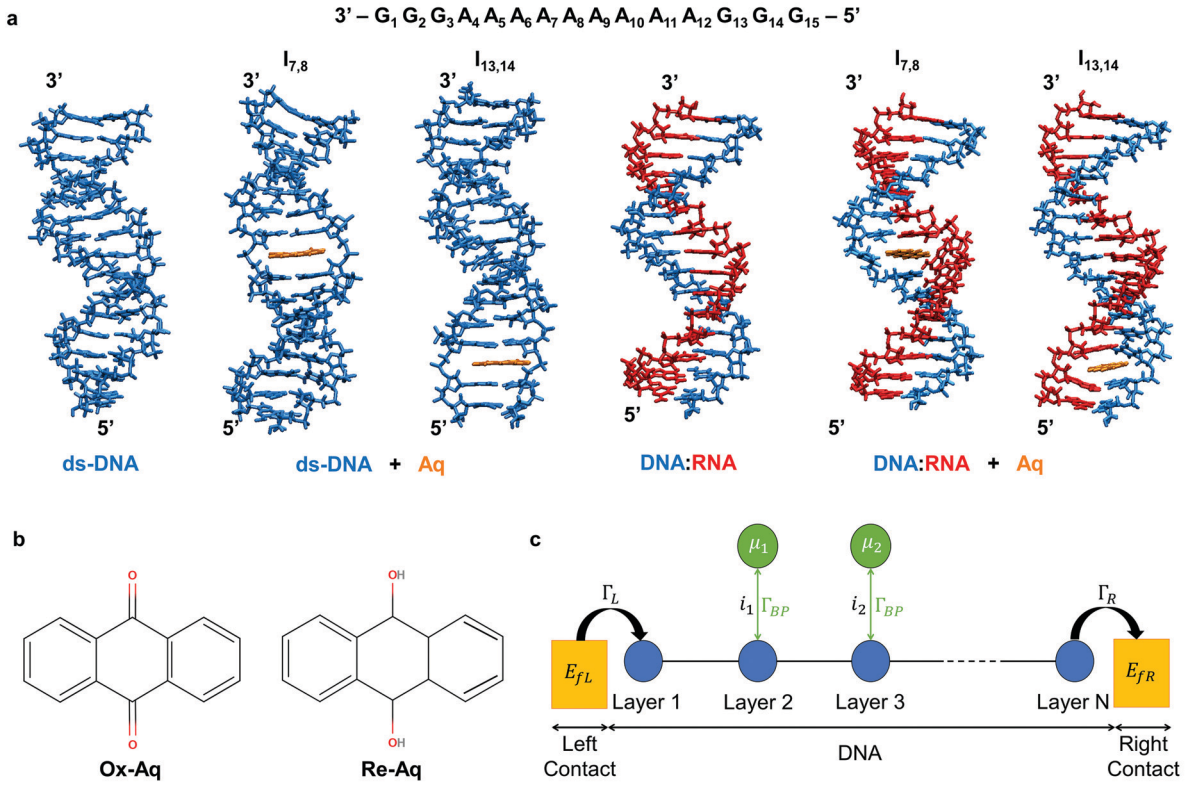


Fig. 1 Schematic representation of the system: (a) Simulated intercalation cases for the 15 base-pair long structures. (b) Oxidized and reduced states of the Aq molecule. (c) Decoherence model for charge transport calculations.

To account for this, we consider intercalation between (a) AT base pairs at 7 and 8 ($I_{7,8}$) and (b) GC base pairs at 13 and 14 ($I_{13,14}$) among other possibilities (Fig. 1). We simulate ds-DNA with and without the intercalator using NAMD[43] with the CHARMM 36 force field.[44] We choose representative structures after more than 80 ns MD simulations (see ESI† methods). In both cases, oxidized and reduced state Aq are studied, called hereafter Ox-Aq and Re-Aq for brevity. As for the DNA:RNA system, the hybrid structure is built using the Amber NAB tool,[45,46] and then Ox-Aq is also intercalated at $I_{7,8}$ and $I_{13,14}$ (see ESI† methods). For this system, we additionally consider Aq conjugated with neomycin acting as a groove binder (AqNEO) to study its effect on charge transport. We use AMBER with the ff99OL3[47,48] and Bsc1[49] force fields to simulate the DNA:RNA system and used the clustering method to choose a representative structure from 50 ns MD simulations. DFT calculations are then carried out using the Gaussian 16[50] software package with the B3LYP/6-31G(d,p) basis set together with the polarizable continuum model. After obtaining the Hamiltonian from the DFT results, charge transport calculations are performed for a system consisting of a contact–DNA–contact configuration (Fig. 1c). The model is based on the Green's function method with probes to include decoherence (see the ESI† for further details).

Structural analysis

We choose representative structures from each MD simulation *via* the RMSD-based clustering analysis of the trajectories for the quantum mechanical calculations (Fig. S1–S4, ESI†). The structural changes in these representative structures upon intercalation are studied using root mean square deviation (RMSD) calculations and structure dendrograms generated using RMSD matrices and the Agnes function (Fig. S5, ESI†), a hierarchical clustering algorithm.[51] We find that the intercalation at the $I_{13,14}$ position causes a smaller structural change compared to the $I_{7,8}$ position. We also observe that intercalation into the middle of the structure causes base flip-out and base sliding in DNA:RNA for both the Ox-Aq-$I_{7,8}$ and AqNEO-$I_{7,8}$ cases (Fig. S6, ESI†). This is consistent with our expectation that intercalation-induced stress closer to the ends can be relaxed more easily. While it changes the total charge of the system, the π–π interactions of the DNA:RNA bases are modulated to a small extent compared to intercalation. Our simulations demonstrate an increase in the binding affinity of the intercalator when conjugated with neomycin (Table S1, ESI†). The structural comparison of Aq- and AqNEO-intercalated DNA:RNA hybrids shows that the duplex structures are similar when intercalated at the $I_{13,14}$ position (RMSD: 0.87 Å); however, when intercalated at the $I_{7,8}$ position (RMSD: 2.32 Å) the conjugated tail part causes relatively higher structural differences (Fig. S5b, ESI†).

Quantum mechanical modeling

An essential effect of Aq intercalation on DNA is in the HOMO and LUMO spatial distribution. Without intercalation, the

Published on 08 June 2021. Downloaded by University of Washington on 9/13/2024 10:54:56 PM.

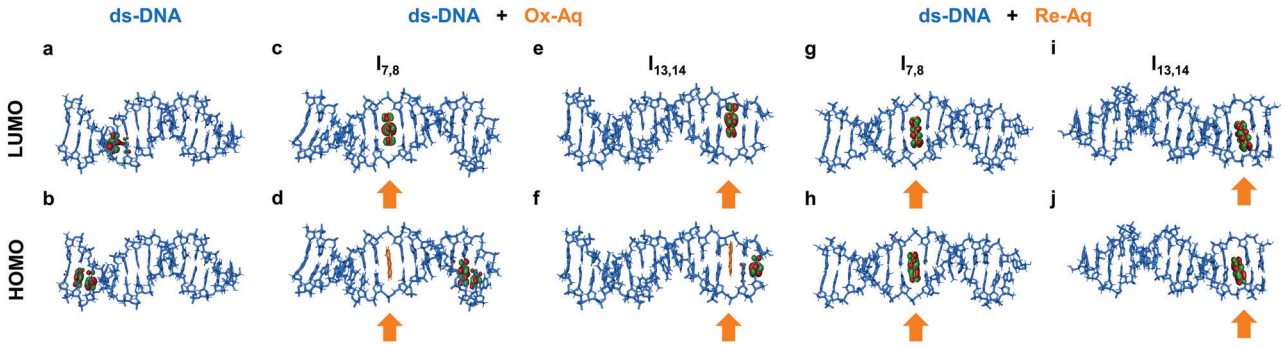


Fig. 2 LUMO and HOMO plots both without and with Aq (the ISO value is 0.02). (a and b) LUMO and HOMO distribution of ds-DNA. (c and d) LUMO and HOMO distribution of ds-DNA intercalated with Ox-Aq between the 7th and 8th base pairs. (e and f) LUMO and HOMO distribution of ds-DNA intercalated with Ox-Aq between the 13th and 14th base pairs. (g and h) LUMO and HOMO distribution of ds-DNA with the same intercalation position as (c and d) using Re-Aq. (i and j) LUMO and HOMO distribution of ds-DNA with the same intercalation position as (e and f) using Re-Aq.

LUMO is localized at a single thymine (Fig. 2a), whereas its HOMO is delocalized on two guanines (Fig. 2b). However, when Ox-Aq is introduced into the system, its effect is seen as adding a new unoccupied level (LUMO) localized at Aq. This result is true for both the $I_{7,8}$ and $I_{13,14}$ cases (Fig. 2c and e). As for the HOMO, it is still localized at the guanines (Fig. 2d and f). However, in the Re-Aq case, both the HOMO and LUMO are localized at Aq (Fig. 2g–j). Therefore, it adds two energy levels into the bandgap as opposed to Ox-Aq. The added levels for Re-Aq (Ox-Aq) near the HOMO (LUMO) are fully occupied (empty). Hence, this is not like the conventional doping of semiconductors where p-doping (n-doping) has unoccupied (occupied) levels induced near the HOMO (LUMO) band. The bandgap value changes as the intercalator adds new energy levels into the DNA. In the Ox-Aq case, the LUMO induced by Aq is seen in the middle of the bandgap closer to the LUMO region of ds-DNA (Fig. 3a). The bandgap is reduced by more than 1.2 eV, from 3.67 eV of bare DNA to 2.12 eV for $I_{7,8}$ and 2.45 eV for $I_{13,14}$. Re-Aq induces two new levels in the bandgap region, a HOMO and a LUMO, which also decrease the bandgap compared with the bare DNA, to 2.97 eV and 2.86 eV for $I_{7,8}$ and $I_{13,14}$ intercalations, respectively. Similar trends are observed for the DNA:RNA system (Fig. S7, ESI†). We observe the LUMO localizing on the intercalating molecule in both the Aq and AqNEO cases. As for the HOMO, it remains localized on the guanines. The bandgap is reduced by 1.48 eV for the Aq case and by 1.66 eV with AqNEO (Fig. 3b). We also notice that the incorporation of neomycin as a groove binding molecule does not significantly alter the molecular orbitals of the system in the HOMO region (AqNEO cases in Fig. 3b). However, the LUMO region is shifted to lower energies for the AqNEO cases. The average shift in the induced energy between the Aq and AqNEO cases is 175 meV. Thus, we find that the groove binder neomycin does not cause a significant effect on the molecular orbitals of the system or the intercalator induced energy levels. In the following section, we explore the transport calculation results for the different cases, specifically at the induced energy levels.

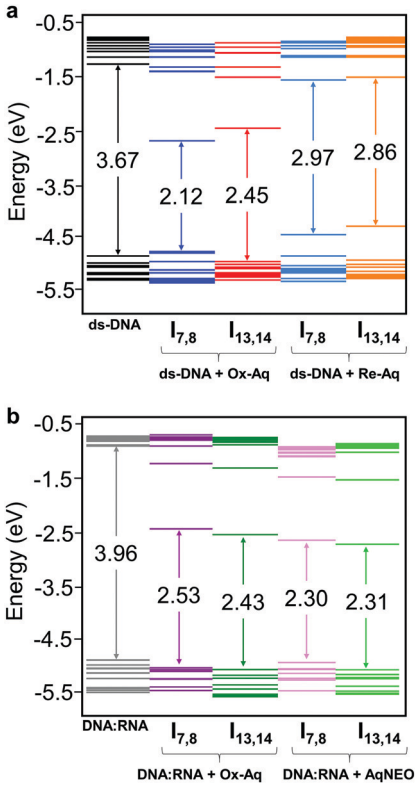


Fig. 3 Energy levels and bandgap values for different intercalation cases of ds-DNA and DNA:RNA. (a) Energy levels for the ds-DNA system. Ox-Aq induces a LUMO into the bandgap of DNA, while Re-Aq induces both a HOMO and LUMO which are close to the energy levels of the DNA, respectively. (b) Energy levels for the DNA:RNA system with the Ox-Aq and AqNEO cases. Both Ox-Aq and AqNEO induce a LUMO into the bandgap of DNA:RNA.

Transmission at the induced levels

Direct comparisons between the original states of ds-DNA and DNA:RNA are discussed in prior ref. 52 and 53. In this work, we focus on the intercalator's effect on charge transport in the ds-DNA and DNA:RNA systems (Fig. S8, ESI†). The transmission is plotted as a function of energy ranging from −6 to 0 eV in Fig. S9–S11 (ESI†). Fig. 4 shows the transmission near the intercalator induced energy levels. The transmission increases at the Aq-induced energy levels by 16–34% compared to bare

 This journal is © The Royal Society of Chemistry 2021

Published on 08 June 2021. Downloaded by University of Washington on 9/13/2024 10:54:56 PM.

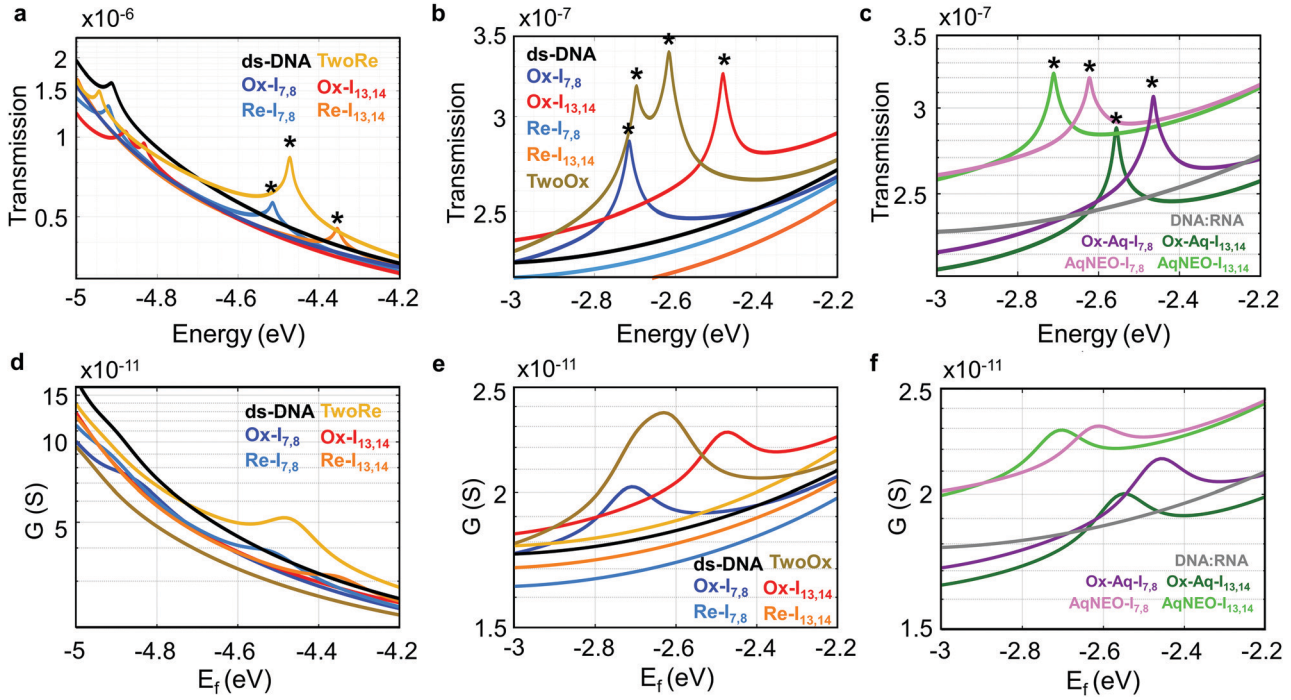


Fig. 4 Transmission plots for (a) the ds-DNA system in the HOMO region (stars: Re-Aq induced peaks), (b) the ds-DNA system in the Aq-induced region (stars: Ox-Aq induced peaks) and (c) the DNA:RNA system in the Aq-induced region (stars: Aq and AqNEO induced peaks). The x-axis is energy because these results do not depend on the occupancy or Fermi factor of the electrons. Conduction plots for (d) ds-DNA in the HOMO region, (e) ds-DNA in the Aq-induced region and (f) DNA:RNA in the Aq-induced region.

DNA (see transmission at the starred peaks in Fig. 4). The Re-Aq cases ($I_{7,8}$ and $I_{13,14}$ in Fig. 4a) show a $\sim$16% increase, whereas Ox-$I_{7,8}$ and Ox-$I_{13,14}$ increase the transmission by 23% and 34%, respectively (Fig. 4b). Similarly, the DNA:RNA system with AqNEO (Aq) exhibits the same trend (Fig. 4c): the intercalator-induced peaks increase the transmission at their respective energies compared to the bare system. It is essential to mention that the induced peaks for Aq (or AqNEO) in its oxidized state are deep in the bandgap region of the no intercalation cases, -2.8 eV $<$ energy $<$ -2.4 eV (Fig. 4b and c and Fig. S9 and S10, ESI†). This range is more than 1.5 eV above the anticipated Fermi energy (E_f) location, which is assumed to be in the HOMO vicinity.

We expect that the closer the Aq-induced levels get to the high density of states (DOS) region, the higher the transmission becomes. This is due to the enhanced coupling of Aq to neighboring bases. The location of intercalation has a small effect on the induced energy levels as shown in Fig. 3. For instance, changing the Ox-Aq location from $I_{7,8}$ to $I_{13,14}$ induces an energy shift of 245 meV, and the corresponding increase in the transmission peak is $\sim$14%. As for Re-Aq, it induces an occupied level close to the HOMO vicinity. Here, Re-$I_{7,8}$ has its HOMO energy level closer to the HOMO of Re-$I_{13,14}$ by 163 meV, and this results in a $\sim$25% increase in the transmission peak (Fig. 4). As for the DNA:RNA system with Aq, Fig. 4c shows that, by changing the location of intercalation from $I_{7,8}$ to $I_{13,14}$, the induced level shifts by 91 meV closer to the LUMO region, only increasing the transmission peak by 7%. On the other hand, in the neomycin conjugate (AqNEO) case, the induced level shifts by 89 meV away from the LUMO. However, this opposite shift yields a change in the transmission peak of less than 1%. We find that the transmission is not affected by the addition of the groove-binder, which is in qualitative agreement with experiments[34,35] that find that groove-binding molecules have an insignificant impact on DNA conductance.

Although we observe that the energy shifts and transmission peaks can quantitatively vary, the percentage of transmission increase in the no-intercalation cases is not significant. These results indicate that the spatial location of intercalation alone cannot be the reason behind the intercalation induced conductance differences reported in the literature. We also considered a hopping model, which supports this conclusion (Fig. S12–S14, ESI†). Thus, in the next section, we will look at the effect of having double intercalation. We would also like to note that, since the effect of intercalation yields similar trends regardless of the system (ds-DNA or DNA:RNA), the following sections will focus on the ds-DNA system.

Double intercalation

Multiple intercalations may occur in experiments depending on the intercalator molecule concentration and the length of the DNA strand.[54,55] We intercalate two anthraquinone molecules into pre-stretched target positions corresponding to the $I_{7,8}$ and $I_{13,14}$ positions. Following this, we minimize and equilibrate the system with MD simulations.

Published on 08 June 2021. Downloaded by University of Washington on 9/13/2024 10:54:56 PM.

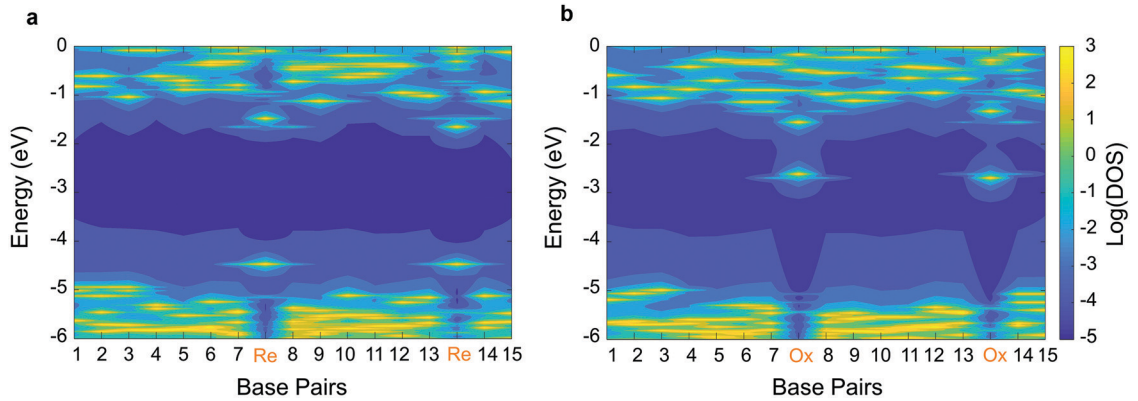


Fig. 5 Double-intercalation effect on the transport properties of ds-DNA. (a) The 2D DOS plot of double Re-Aq, and (b) the 2D DOS plot of double Ox-Aq, showing the energy level distributions along the strand.

The transmission results show that, in the Re-Aq case, a single transmission peak occurs near the HOMO region for double intercalators (TwoRe), which is ~83% higher than the single intercalation cases (Fig. 4a). However, in the Ox-Aq case, the double-intercalation (TwoOx) yields two transmission peaks close in amplitude to the single intercalation cases (Fig. 4b).

To understand this, we look at the 2D DOS plot. The plot shows the distribution of electrons as a function of both space and energy. Fig. 5a shows that the two intercalators induce two nearly degenerate levels near the HOMO region of the DNA for the Re-Aq case. Hence, having higher coupling with the neighboring bases of the DNA, they yield a large transmission peak. However, in the Ox-Aq case, the energy levels are deep in the bandgap region (dark blue area in Fig. 5b). Therefore, they are residing in an almost isolated region with low coupling to the DNA bases. Hence, increasing the number of Re-Aq intercalators can yield higher transmission probability at the induced levels.

So far, we have focused our discussion on the Aq-induced levels. The calculations show that the induced energy levels inside the bandgap cause a transmission increase of less than 45% for this 15 base-pair long strand. At the same time, a higher percentage increase is reached with double-intercalators. Compared with the literature, in which a more than three times increase was reported, we deduce that the induced levels cannot be the only factor in increasing the DNA conductance. To probe other mechanisms that may influence the conductance, in the next section, we look at the overall conductance profile of the ds-DNA cases in different energy regions.

Conductance and Fermi energy location

In this section, we present results for two types of modelling scenarios: ds-DNA is connected between two electrodes with and without a gate electrode system, respectively named the three-terminal and the two-terminal scenarios. In the three-terminal case (Fig. 6b), the Fermi energy is swept between the HOMO and LUMO energies using a gate electrode (Fig. 6b). In the two-terminal case (Fig. 8b) we estimate the Fermi energy location. We assumed that the electrodes are coupled to the DNA ends *via* thiol linker groups in both experiments, which is the common approach in STM-break junction setups.[56,57] This assumption provides us with the information that for small biases we operate in the linear response regime[4,58,59] (where most of the potential drop occurs across the electrode–thiol linker junction). However, we have not explicitly included the thiol linkers or the electrodes due to the enormous computational complexity. More details are available in the ESI† about the transport calculations.

(1) Three-terminal scenario (Fermi energy sweep). Here, we assume a fixed small bias applied to the molecule while we sweep the Fermi energy *via* a third gate electrode and calculate the conductance. The conductance plot is shown in Fig. 6a as a function of E_f, where we shifted the HOMOs of all molecules to match. If the Fermi energy is at the HOMO for each case (or the HOMO plus a few hundred meV), it is apparent that the conductance is largest for oxidized Aq (Ox-$I_{13,14}$), followed by bare DNA and the two remaining oxidized cases. In contrast, the Re-Aq cases have the lowest conductance values. The reason behind this is that the HOMO of the Re-Aq cases is localized at Aq, whereas it is localized at the DNA strand for Ox-Aq (see Fig. 2). Therefore, we predict that the three-terminal experiments should result in this conductance trend when E_f is close to the HOMO of each structure.

In contrast to sweeping the Fermi energy, in the next section we explore a broader approach by estimating the location of the Fermi energy for each case using the principle of partial charge transfer.

(2) Two-terminal scenario (Fermi energy location). The second type of modelling scenario involves a two-terminal setup (without a gate). Here, we do not know where the contact's Fermi energy lies *a priori*, but it is determined *via* the partial charge transfer method. In molecular junctions, it is known that the nature of the interface (gold electrode/ds-DNA) affects the Fermi energy of the contact. The adsorption of the molecule to the contacts causes both broadening of the molecular energy levels and partial charge transfer. Both the geometry and the orientation of the gold contacts may affect the amount of broadening and charge transfer within the molecular system

 This journal is © The Royal Society of Chemistry 2021

Published on 08 June 2021. Downloaded by University of Washington on 9/13/2024 10:54:56 PM.

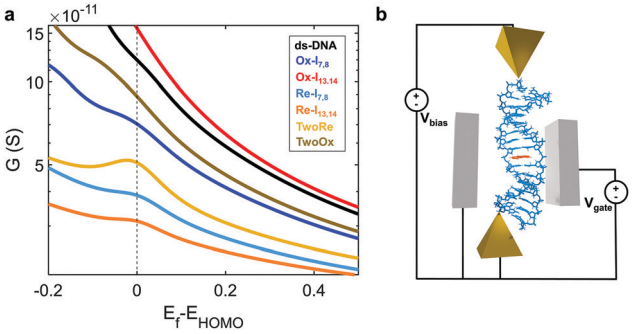


Fig. 6 (a) Conductance plot as a function of Fermi energy for the ds-DNA intercalation cases with all HOMOs aligned (dashed line). (b) Three-terminal scenario.

under study. Including these effects in the calculations will, in principle, allow the evaluation of the Fermi energy position. This approach has been utilized previously on small molecules resulting in a wide range of Fermi energy locations extending from the HOMO to the LUMO.[60] Given this and the difficulty of including gold contacts for studying a molecule of more than a thousand atoms,[61] we take an alternate approach proposed by Zahid and collaborators.[60] They suggested taking the Fermi energy rather as a fitting parameter for calculations of molecular shifts due to partial charge transfer.

In the DNA–contact system, we expect a shift in the molecular energy levels with respect to the Fermi energy of the gold contacts. Partial charge transfer occurs from the contact to the DNA, shifting the MOs to higher energies. E_f is in general closer to the HOMO than to the LUMO. Our approach here is to estimate E_f using the rate of change in energy as we vary the number of electrons in the system within the bandgap region. The higher the rate, the higher the shift in the MOs, and the closer the HOMO gets to E_f. To achieve this, we first estimate the number of electrons in the bandgap region (Fig. S15, ESI†) by integrating the local density of states (LDOS) using a Green's function as:

$$\begin{aligned} N(E_i) &= \iint \mathrm{LDOS}(x,E) f(E-E_i)\mathrm{d}x\mathrm{d}E \\ &= \frac{1}{\pi}\iint -\mathrm{Im}[\mathrm{diag}(G^r)] f(E-E_i)\mathrm{d}x\mathrm{d}E \end{aligned} \quad (1)$$

where x represents the location of the atoms in the system, and $f(E-E_i)$ is the Fermi-function, which describes the probability of electron occupancy at energy E when $E_f = E_i$. After obtaining N *versus* E_i, we calculate the derivative ($\mathrm{d}E_i/\mathrm{d}N$), which gives us the average change in energy $\mathrm{d}E_i$ for a small change in electron number $\mathrm{d}N$ (Fig. S16, ESI†). The average change per one electron for each case is listed in Table 1. The values show that the Ox-Aq cases have the lowest rates, by an average difference of 0.81 eV per electron from bare DNA. The Re-Aq cases have a higher rate than the bare DNA by an average of 0.47 eV per electron. This trend can explain how partial charge transfer affects each case. When the same amount of partial charge is transferred from the gold contact to DNA: (1) Ox-Aq has the lowest shift of the molecular orbitals, which translates to E_f being the farthest from the HOMO region. (2) Re-Aq has the largest shift, making E_f the closest to the HOMO. (3) Bare DNA is between the Ox-Aq and Re-Aq cases.

Table 1 Average rate of change in energy with respect to the number of electrons for ds-DNA

Molecule	$\mathrm{d}E_i/\mathrm{d}N$ (eV per electron)	Change
TwoOx	2.61	−0.93
Ox-$I_{7,8}$	2.61	−0.93
Ox-$I_{13,14}$	2.97	−0.57
ds-DNA	3.54	0
TwoRe	3.75	0.21
Re-$I_{7,8}$	4.13	0.59
Re-$I_{13,14}$	4.16	0.62

Therefore, we can estimate the location of E_f by incrementing the amount of partial charge transfer ($\mathrm{d}N$), using the following equation:

$$E_f = E_{f_0} - \left(\frac{\mathrm{d}E_i}{\mathrm{d}N}\right) \times \mathrm{d}N \quad (2)$$

where E_{f_0} represents the Fermi energy of the electrode before making the contact–molecule junction, $\mathrm{d}E_i/\mathrm{d}N$ is taken from Table 1, $\mathrm{d}N$ is a sweeping parameter, and E_f is the location of the Fermi energy after the MO shift due to the partial charge transfer. We assumed different starting points for E_{f_0}, and extracted the conductance of each case at their respective E_f. Next, we compared the conductance values with the bare DNA case, and the ratios are plotted in Fig. 7. We plotted the conductance ratio for each case as a function of partial charge transfer ($\mathrm{d}N$) for $E_{f_0} = -3.5$ eV in Fig. 7a (Fig. S17 and S18, ESI,† for −3.0 eV, −3.2 eV, −3.5 eV, and −4.0 eV). Notice how at $\mathrm{d}N > 0$ the conductance ratios for TwoRe and Re-$I_{13,14}$ become greater than 1, while Re-$I_{7,8}$ needs $\mathrm{d}N > 0.2$ electrons to reach ratios greater than 1. As for the Ox-Aq cases, the ratios are below 1 for $\mathrm{d}N > 0$.

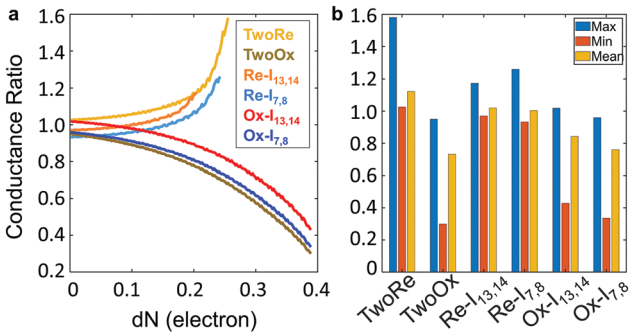


Fig. 7 Conductance ratio with respect to ds-DNA for the different intercalation cases. (a) Conductance ratio as a function of partial charge transfer for $E_{f_0} = -3.5$ eV. The conductance is extracted at each E_f value based on eqn (2) and compared with the conductance of ds-DNA without an intercalator. The cut-offs seen in some curves near 0.25 electrons (Re-Aq cases) are because E_f has reached the respective HOMO, which is set as the cut-off for incrementing $\mathrm{d}N$. (b) The maximum, minimum, and average values are taken for a $\mathrm{d}N$ range going from 0.001 electrons to 0.4 electrons.

Published on 08 June 2021. Downloaded by University of Washington on 9/13/2024 10:54:56 PM.

Fig. 7b summarizes the results for the different cases. The results are consistent for the different E_{f_0} cases and show a maximum increase in conductance of ~1.6 times for Re-Aq, with an average ratio higher than bare DNA. The Ox-Aq cases have average ratios of less than 1. These results are at least qualitatively consistent with the conductance measurements reported in the literature,[36] which show that $G(E_f^{\text{Re-Aq}}) > G(E_f^{\text{DNA}}) > G(E_f^{\text{Ox-Aq}})$; however, the structure in the reference is for a different Aq-based strand. An example graph is plotted in Fig. 8a for dN = 0.2 eV and E_{f_0} = −3.5 eV values showing $G(E_f^{\text{Re-Aq}}) > G(E_f^{\text{DNA}}) > G(E_f^{\text{Ox-Aq}})$.

To summarize, the location of E_f for the DNA does impact the conductance ratios between bare DNA and DNA + Aq. The present analysis shows that the E_f values of the Re-Aq intercalation cases are closer to the HOMO region than E_f of bare DNA. As a result, the conductance can be as high as 1.6 times for the DNA + TwoRe case (Fig. 7b). In contrast, we find E_f to be farther away from the HOMO in the Ox-Aq cases, and the conductance is lower than bare DNA. These results indicate that there are two mechanisms in play in increasing the conductance of Re-Aq intercalated DNA: (1) a Fermi energy shift, and (2) induced energy levels above the HOMO to help traverse the AT region.

Effect of the AT region length

In this section, we study a strand with a shorter AT-region to investigate the effect of the AT region length on the Aq-induced energy levels and the conductance. Here, we simulate the 3′-GGGAAAGGG-5′ strand, with Aq intercalating at $I_{5,6}$, or $I_{7,8}$, and both (two-Aq). The main result is that the Re-Aq induced levels are now closer to the HOMO region of ds-DNA, lowering the energy separation from 500 meV in 3′-G3A9G3-5′ (see Fig. 3a) to less than 70 meV in 3′-G3A3G3-5′ (Fig. S19, ESI†). We attribute this result to the increase in coupling between the two GC regions as well as the intercalated Re-Aq (Fig. S20–S23, ESI†).

The transport calculations in Fig. S24 (ESI†) show that the increase in transmission at the Re-Aq induced levels (−4.75 eV < energy < −4.8 eV) is now higher compared to the longer AT case (Fig. 4). Re-$I_{5,6}$ has two transmission peaks with a more than 3× increase and the two-Aq case has a peak of more than 5× higher transmission than the bare-DNA. The energy of the induced level shifts by 50 meV for Re-Aq when going from Re-$I_{5,6}$ to Re-$I_{7,8}$, and the transmission changes by 30%. Whereas the variation in the Ox-Aq cases is 120 meV and the transmission changes by less than 2.5%.

We also carried out Fermi energy location analysis: (1) a three-terminal scenario where E_f is changed with a gate, and (2) a two-terminal scenario where we estimate the E_f location based on partial charge transfer. For the first scenario, Fig. S25 (ESI†) shows that, for the conductance for E_f at the HOMO (or at a few hundred meV higher energies), the Ox-Aq cases are higher than bare DNA. Furthermore, Re-$I_{5,6}$ is only marginally greater than the bare DNA at the HOMO while it decreases at higher energies, with the remaining two Re-Aq cases displaying lower conductance in general. Again, these findings are due to the localization of the HOMO at Re-Aq, while the HOMO of the oxidized cases is primarily localized on the DNA bases.

As for the second scenario, the calculated dE_i/dN values yield the same trend as the 3′-G3A9G3-5′ structure (Table S3, ESI†). By performing the same conductance ratio analysis, we get a maximum conductance increase of 2.2 for TwoRe, 4.0 for Re-$I_{5,6}$, and 3.0 for Re-$I_{7,8}$, with an overall average ratio greater than 1 (Fig. 9). The ratio drops below 1.0 for different dN values depending on the intercalation location for the oxidized cases. For example, Fig. 9a shows the conductance ratios for the E_{f_0} = −3.5 eV case (for other cases see Fig. S26 and S27, ESI†). Here, TwoOx displays a ratio less than 1.0 at dN > 0, Ox-$I_{7,8}$ drops below 1.0 at dN > 0.1 electrons, and Ox-$I_{5,6}$ drops below 1 at dN > 0.2 electrons. These results confirm that, for the shorter AT-region strand, the location of the intercalation, the number of intercalations, and the partial charge transferred have an important effect on the conductance of the DNA. The general trend, however, is still $G(E_f^{\text{Re-Aq}}) > G(E_f^{\text{DNA}}) > G(E_f^{\text{Ox-Aq}})$.

In summary, the reduced state of the intercalator increases the conductance more significantly as the AT region length decreases. In the shorter case, the intercalator-induced energy levels have lower energy separation from the HOMO level.

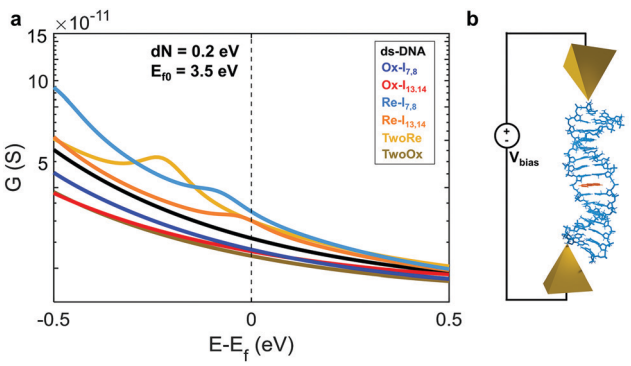


Fig. 8 (a) Example of a conductance plot as a function of Fermi energy for the ds-DNA intercalation cases for chosen dN = 0.2 eV and E_{f_0} = −3.5 eV values, where E_f is calculated using eqn (2). (b) Two-terminal scenario.

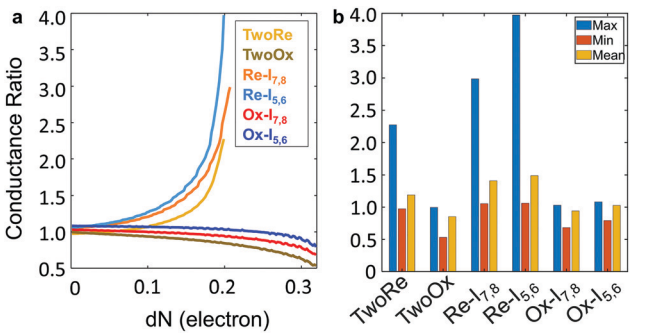


Fig. 9 Conductance ratio with respect to ds-DNA for the different intercalation cases (3′-G3A3G3-5′). (a) Conductance ratio as a function of partial charge transfer for E_{f_0} = −3.5 eV. The conductance is extracted at each E_f value based on eqn (2) and compared with the conductance of ds-DNA without an intercalator. The cut-offs seen in some curves near 0.2 electrons (Re-Aq cases) are because E_f has reached the respective HOMO, which is set as the cut-off for incrementing dN. (b) The maximum, minimum, and average values are taken for a dN range going from 0.001 electrons to 0.31 electrons (see the ESI† for more E_{f_0} cases).

This journal is © The Royal Society of Chemistry 2021

Published on 08 June 2021. Downloaded by University of Washington on 9/13/2024 10:54:56 PM.

Therefore, they help increase the coupling between the GCs on the two sides of the DNA. This finding is consistent for any amount of partial charge transfer. Ox-Aq causes the DNA conductance to decrease, and the decrease is more sensitive to the amount of charge transfer and the intercalation location compared to Re-Aq.

Conclusions

In this paper, we investigated the effect of Aq-intercalation on the conductance of nucleic acids, ds-DNA and a DNA:RNA hybrid, through a combination of molecular dynamics, *ab initio* simulations, and charge transport calculations. We find the intercalation to yield similar effects on the DNA:RNA hybrid system. The DNA:RNA + AqNEO analysis shows that the groove binding molecule increases the stability of the molecular structure while having a small effect on the molecular energy levels and conductance compared to the intercalators. Thus, an important finding of this work is that one can use a groove binder conjugated to the intercalator to increase the system's overall structural stability[39,40] without affecting the electronic properties induced by the intercalator, a crucial feature for the thermal stability of future DNA based molecular devices. We showed that intercalation can modulate the conductance of ds-DNA. One can control this by using parameters such as the redox state of the intercalator, the location of the Fermi energy, and the length of the strand.

Our results show that, although Aq induces energy levels in the bandgap of the ds-DNA, this is not like the conventional doping in semiconductors. The added levels for Re-Aq (Ox-Aq) near the HOMO (LUMO) are occupied (empty). Therefore, the electrons must travel through these induced energy levels to traverse the structure, as they do not increase the number of charge carriers in the system. In addition to the induced energy levels in the bandgap, the contact's Fermi energy with respect to the molecule modifies the conductance. The Fermi energy analysis shows that Aq can either increase or decrease the DNA conductance based on its redox state. Re-Aq was assessed to have the Fermi energy closest to the HOMO region, with Ox-Aq having it the farthest away from the HOMO, hence yielding the relation $G(E_f^{\text{Re-Aq}}) > G(E_f^{\text{DNA}}) > G(E_f^{\text{Ox-Aq}})$ with maximum conductance 1.6 times higher (TwoRe) than the bare DNA. This relation agrees with the experiment conducted,[36] where they have shown that the DNA conductance can increase or decrease based on the state of anthraquinone. Furthermore, lowering the AT-region length from 9 base pairs to 3 increases the impact of Re-Aq, yielding a maximum conductance rise of 2.5 times for two intercalators and a more than 4.0 times increase for a single intercalator. This means that increasing the number of intercalators does not always yield enhanced conductance, especially for shorter strands. Our results also show that the experimental setup may alter the measured conductance. In the three-terminal case, where the gate voltage is swept, the Ox-Aq intercalation yields higher conductance than the Re-Aq intercalation case, when the relative Fermi energy locations with respect to the HOMO levels are the same. Overall, we demonstrated that one can modulate the conductance by altering the number of intercalators, the AT-region length, and/or the experimental setup. A possible application for intercalation in addition to modulating nucleic acid conductance arises from utilizing multiple intercalators with different redox potentials (such as ethidium bromide), which in principle can help to create a multi-level gating effect for the same strand.

Conflicts of interest

There are no conflicts to declare.

Acknowledgements

We acknowledge NSF ECCS Grant Number 1807391 and 1807555 and SRC grant number 2836l. H Mohammad further acknowledges a Kuwait University fellowship. We acknowledge using the Hyak supercomputer system at the University of Washington and TUBITAK ULAKBIM, High Performance and Grid Computing Center (TRUBA resources).

Notes and references

1 R. G. Endres, D. L. Cox and R. R. P. Singh, *Rev. Mod. Phys.*, 2004, **76**, 195–214.
2 E. Wierzbinski, A. De Leon, X. Yin, A. Balaeff, K. L. Davis, S. Reppireddy, R. Venkatramani, S. Keinan, D. H. Ly, M. Madrid, D. N. Beratan, C. Achim and D. H. Waldeck, *J. Am. Chem. Soc.*, 2012, **134**, 9335–9342.
3 M. Xu, R. G. Endres and Y. Arakawa, *Small*, 2007, **3**, 1539–1543.
4 J. Qi, N. Govind and M. P. Anantram, *J. Chem. Phys.*, 2015, **143**, 094306.
5 Y. Zhang, R. M. Young, A. K. Thazhathveetil, A. P. N. Singh, C. Liu, Y. A. Berlin, F. C. Grozema, F. D. Lewis, M. A. Ratner, N. Renaud, K. Siriwong, A. A. Voityuk, M. R. Wasielewski and D. N. Beratan, *J. Phys. Chem. Lett.*, 2015, **6**, 2434–2438.
6 J. M. Artés, Y. Li, J. Qi, M. P. Anantram and J. Hihath, *Nat. Commun.*, 2015, **6**, 1–8.
7 C. Adessi, S. Walch and M. P. Anantram, *Phys. Rev. B: Condens. Matter Mater. Phys.*, 2003, **67**, 1–4.
8 C. Bruot, L. Xiang, J. L. Palma and N. Tao, *ACS Nano*, 2015, **9**, 88–94.
9 Y. Li, J. M. Artés, B. Demir, S. Gokce, H. M. Mohammad, M. Alangari, M. P. Anantram, E. E. Oren and J. Hihath, *Nat. Nanotechnol.*, 2018, **13**, 1167–1173.
10 H. Mehrez and M. P. Anantram, *Phys. Rev. B: Condens. Matter Mater. Phys.*, 2005, **71**, 115405.
11 T. Bayrak, S. Helmi, J. Ye, D. Kauert, J. Kelling, T. Schönherr, R. Weichelt, A. Erbe and R. Seidel, *Nano Lett.*, 2018, **18**, 2116–2123.
12 Y. Zhang, S. Z. Chen, Z. X. Xie, X. Yu, Y. X. Deng, X. H. Chen and F. Ning, *Phys. Lett. Sect. A Gen. At. Solid State Phys*, 2019, **383**, 2069–2075.
13 H. M. J. Al-Ta'ii, V. Periasamy and Y. M. Amin, *Sens. Actuators, B*, 2016, **232**, 195–202.

Published on 08 June 2021. Downloaded by University of Washington on 9/13/2024 10:54:56 PM.

14 M. Yoon, S. W. Min, S. R. Dugasani, Y. U. Lee, M. S. Oh, T. D. Anthopoulos, S. H. Park and S. Im, *Small*, 2017, **13**, 1703006.
15 J. Lee, J. H. Park, Y. T. Lee, P. J. Jeon, H. S. Lee, S. H. Nam, Y. Yi, Y. Lee and S. Im, *ACS Appl. Mater. Interfaces*, 2014, **6**, 4965–4973.
16 Y. Cho, J. Lee, J. Y. Lim, S. Yu, Y. Yi and S. Im, *J. Phys. D: Appl. Phys.*, 2017, **50**, 065107.
17 L. Kékedy-Nagy and E. E. Ferapontova, *Angew. Chem., Int. Ed.*, 2019, **58**, 3048–3052.
18 K. L. Jiménez-Monroy, N. Renaud, J. Drijkoningen, D. Cortens, K. Schouteden, C. van Haesendonck, W. J. Guedens, J. V. Manca, L. D. A. Siebbeles, F. C. Grozema and P. H. Wagner, *J. Phys. Chem. A*, 2017, **121**, 1182–1188.
19 M. DeLuca, Z. Shi, C. E. Castro and G. Arya, *Nanoscale Horiz.*, 2020, **5**, 182–201.
20 G. R. Abel, L. E. Korshoj, P. B. Otoupal, S. Khan, A. Chatterjee and P. Nagpal, *Chem. Sci.*, 2019, **10**, 1052–1063.
21 T. Furuhata, T. Ohshiro, G. Akimoto, R. Ueki, M. Taniguchi and S. Sando, *ACS Nano*, 2019, **13**, 5028–5035.
22 S. Afsari, L. E. Korshoj, G. R. Abel, S. Khan, A. Chatterjee and P. Nagpal, *ACS Nano*, 2017, **11**, 11169–11181.
23 J. B. Chaires, *Curr. Opin. Struct. Biol.*, 1998, **8**, 314–320.
24 S. Bhaduri, N. Ranjan and D. P. Arya, Beilstein, *J. Org. Chem.*, 2018, **14**, 1051–1086.
25 H. S. Rye, S. Yue, D. E. Wemmer, M. A. Quesada, R. P. Haugland, R. A. Mathies and A. N. Glazer, *Nucleic Acids Res.*, 1992, **20**, 2803–2812.
26 H. M. Berman and P. R. Young, *Annu. Rev. Biophys. Bioeng.*, 1981, **10**, 87–114.
27 J. B. Chaires, *Arch. Biochem. Biophys.*, 2006, **453**, 26–31.
28 H. Lei, X. Wang and C. Wu, *J. Mol. Graphics Modell.*, 2012, **38**, 279–289.
29 A. A. Almaqwashi, T. Paramanathan, I. Rouzina and M. C. Williams, *Nucleic Acids Res.*, 2016, **44**, 3971–3988.
30 L. Maganti and D. Bhattacharyya, *J. Comput.-Aided Mol. Des.*, 2020, **34**, 83–95.
31 W. D. Sasikala and A. Mukherjee, *Phys. Chem. Chem. Phys.*, 2013, **15**, 6446.
32 C. Liu, L. Guo, B. Zhang and L. Lu, *RSC Adv.*, 2019, **9**, 31636–31644.
33 C. Guo, K. Wang, E. Zerah-Harush, J. Hamill, B. Wang, Y. Dubi and B. Xu, *Nat. Chem.*, 2016, **8**, 484–490.
34 T. Harashima, C. Kojima, S. Fujii, M. Kiguchi and T. Nishino, *Chem. Commun.*, 2017, **53**, 10378–10381.
35 X. Wang, L. Gao, B. Liang, X. Li and X. Guo, *J. Mater. Chem. B*, 2015, **3**, 5150–5154.
36 L. Xiang, J. L. Palma, Y. Li, V. Mujica, M. A. Ratner and N. Tao, *Nat. Commun.*, 2017, **8**, 1–10.
37 A. Aggarwal, A. K. Sahoo, S. Bag, V. Kaliginedi, M. Jain and P. K. Maiti, *Phys. Rev. E*, 2021, **103**, 032411.
38 N. N. Degtyareva, C. Gong, S. Story, N. S. Levinson, A. K. Oyelere, K. D. Green, S. Garneau-Tsodikova and D. P. Arya, *ACS Infect. Dis.*, 2017, **3**, 206–215.
39 H. Xi, D. Gray, S. Kumar and D. P. Arya, *FEBS Lett.*, 2009, **583**, 2269–2275.
40 N. N. Shaw, H. Xi and D. P. Arya, *Bioorg. Med. Chem. Lett.*, 2008, **18**, 4142–4145.
41 J. S. Al-Otaibi and P. Teesdale, Spittle and T. M. El Gogary, *J. Mol. Struct.*, 2017, **1127**, 751–760.
42 B. Gatto, G. Zagotto, C. Sissi and M. Palumbo, *Int. J. Biol. Macromol.*, 1997, **21**, 319–326.
43 J. C. Phillips, R. Braun, W. Wang, J. Gumbart, E. Tajkhorshid, E. Villa, C. Chipot, R. D. Skeel, L. Kalé and K. Schulten, *J. Comput. Chem.*, 2005, **26**, 1781–1802.
44 K. Vanommeslaeghe, E. Hatcher, C. Acharya, S. Kundu, S. Zhong, J. Shim, E. Darian, O. Guvench, P. Lopes, I. Vorobyov and A. D. Mackerell, *J. Comput. Chem.*, 2010, **31**, 671–690.
45 D. A. Case, V. Babin and J. T. Berryman, *et al.*, AMBER 14, 2014.
46 D. A. Case, R. M. Betz and D. S. Cerutti, *et al.* AMBER 2016, Univ. California, San Fr.
47 A. Pérez, I. Marchán, D. Svozil, J. Sponer, T. E. Cheatham, C. A. Laughton and M. Orozco, *Biophys. J.*, 2007, **92**, 3817–3829.
48 M. Zgarbová, M. Otyepka, J. Šponer, A. Mládek, P. Banáš, T. E. Cheatham and P. Jurečka, *J. Chem. Theory Comput.*, 2011, **7**, 2886–2902.
49 I. Ivani, P. D. Dans, A. Noy and A. Pérez, *et al.*, *Nat. Methods*, 2016, **13**, 55–58.
50 D. J. Frisch, M. J. Trucks and G. W. Schlegel, *et al.*, *Gaussian 16*, 2016.
51 R Core Team, R Found. Stat. Comput., 2019.
52 Y. Li, J. M. Artés, J. Qi, I. A. Morelan, P. Feldstein, M. P. Anantram and J. Hihath, *J. Phys. Chem. Lett.*, 2016, **7**, 1888–1894.
53 A. Aggarwal, S. Bag, R. Venkatramani, M. Jain and P. K. Maiti, *Nanoscale*, 2020, **12**, 18750–18760.
54 A. Patra and C. Richert, *J. Am. Chem. Soc.*, 2009, **131**, 12671–12681.
55 J. N. Lisgarten, M. Coll, J. Portugal, C. W. Wright and J. Aymami, *Nat. Struct. Biol.*, 2002, **9**, 57–60.
56 B. Kim, J. M. Beebe, Y. Jun, X.-Y. Zhu and C. D. Frisbie, *J. Am. Chem. Soc.*, 2006, **128**(15), 4970–4971.
57 Y. Tsuji, T. Stuyver, S. Gunasekaran and L. Venkataraman, *J. Phys. Chem. C*, 2017, **121**, 14451–14462.
58 B. Xu and N. J. Tao, *Science*, 2003, **301**, 1221–1223.
59 J. Qi, N. Edirisinghe, M. G. Rabbani and M. P. Anantram, *Phys. Rev. B: Condens. Matter Mater. Phys.*, 2013, **87**, 085404.
60 F. Zahid, M. Paulsson and S. Datta, *Advanced Semiconductor and Organic Nano-Techniques*, Elsevier Inc., 2003, pp. 1–41.
61 L. E. Ratcliff, S. Mohr, G. Huhs, T. Deutsch, M. Masella and L. Genovese, *Wiley Interdiscip. Rev.: Comput. Mol. Sci.*, 2017, **7**, e1290.

 This journal is © The Royal Society of Chemistry 2021